Eur. Phys. J. D **36**, 79–88 (2005)
DOI: 10.1140/epjd/e2005-00197-2

THE EUROPEAN
PHYSICAL JOURNAL D

Experimental studies of complex crater formation under cluster implantation of solids

S. Prasalovich[1], V. Popok[1,a], P. Persson[2], and E.E.B. Campbell[1]

[1] Department of Physics, Göteborg University, 41296 Göteborg, Sweden
[2] Department of Physics and Measurement Technology, Linköping University, 58183 Linköping, Sweden

Received 21 March 2005
Published online 26 July 2005 – © EDP Sciences, Società Italiana di Fisica, Springer-Verlag 2005

Abstract. The results of a systematic study of surface defect formation after energetic Ar_n^+ ($n = 12, 22, 32, 54$) and Xe_n^+ ($n = 4, 16$) cluster ion implantation into silicon and sapphire are presented. Implantation energies vary from 3 to 18 keV/ion. Two cases of comparative studies are carried out: the same cluster species are implanted into two different substrates, i.e. Ar_n^+ cluster ions into silicon and sapphire and two different cluster species Ar_n^+ and Xe_n^+ are implanted into the same kind of substrate (silicon). Atomic force, scanning electron and transmission electron microscopies (AFM, SEM and TEM) are used to study the implanted samples. The analysis reveals the formation of two types of surface erosion defects: simple and complex (with centrally positioned hillock) craters. It is found that the ratio of simple to complex crater formation as well as the hillock dimensions depend strongly on the cluster species, size and impact energy as well as on the type of substrate material. Qualitative models describing the two comparative cases of cluster implantation, the case of different cluster species and the case of different substrate materials, are proposed.

PACS. 61.46.+w Nanoscale materials: clusters, nanoparticles, nanotubes, and nanocrystals – 61.80.Lj Atom and molecule irradiation effects – 68.37.-d Microscopy of surfaces, interfaces, and thin films

1 Introduction

Clusters of atoms and molecules have been intensively studied during the last twenty years in different fields of science and technology because of their unique properties. For example, beams of clusters are considered to be powerful and versatile tools for modification of solids. Deposition of clusters, thin film growth, cluster implantation, surface smoothing and etching by cluster beams are the main application oriented directions stimulating research in this field [1–7]. Such a broad interest in cluster beams is due to the possibility of transporting matter in a controllable fashion which allows the synthesis and processing of structures on the nm-scale.

Cluster-surface impact is fundamentally different from that of monomer ion impact. Clusters generate multiple-collision effects and their interaction with the substrate is non-linear. Non-linearity arises from the fact that many-particle interactions have to be taken into account and the simple binary collision theory doesn't work properly in most of the cases when describing the stopping of clusters in solids. It is therefore of interest to study the effect of single cluster-surface impact in both experiment and theory. Through understanding such fundamental aspects one can hope to develop more applied research and make use of the full power of cluster beams for producing novel nanostructured materials.

Energetic cluster impact with low ion fluences typically produces two main types of defects on the surface: craters and hillocks. Both of these features have been known before for conventional monomer ion implantation. One of the first observations of crater formation after heavy ion sputtering was published in the beginning of the 1980s [8]. A thermal spike model [9, 10] was used to explain the crater formation associated with individual displacement cascades originated by the penetrating particles. Along with craters, bumps with heights of a few nm, called hillocks, were also found in experiments on ion-surface collisions [11, 12]. The ion impact energies at which this effect was observed were in the keV range. Later on, the same features were also revealed in different experiments involving low energy multiply charged ions [13] as well as swift heavy ions [14–16]. In most cases the origin of the hillocks is explained in terms of the above mentioned thermal spike model. Thus, for low energy implantation, when nuclear stopping of the projectile ion is dominant, the spike is thought to result from the energy deposited by ion-atom and atom-atom collisions during the ballistic phase of the collision cascade in the target. With an increase of implantation energy (MeV and higher), the

[a] e-mail: popok@fy.chalmers.se

role of energy loss due to electronic excitation along the track increases and the contribution from the electronic stopping to the spike energy dominates over the nuclear stopping. In this case the hillock height is an increasing function of the implantation energy [17].

During the last ten years some experimental studies were performed on crater formation by cluster ions for different energy regimes, cluster sizes and substrate materials [18, 19]. This research was accompanied by MD simulations where various empirical potentials were employed [18, 20, 21]. In the case of cluster implantation, MD simulations treat all the cluster atoms simultaneously, in this way accounting for non-linear effects to some extent. For impact normal to the surface, craters are typically observed in MD simulations to be hemispherical in shape. In some cases the crystallographic structure can be reflected in the asymmetry of the crater wall [18] and with a change of impact angle the crater shape follows the direction of the beam in which direction also the maximum sputtering occurs [1, 22]. Because of the effective material excavation by impacting clusters, the formation of crater rims with heights that can reach ca. one nm was observed [18, 23].

It was shown by both experiment and theory that stopping of a cluster ion consisting of n atoms is not necessarily the same as n times the stopping of one individual ion, or more precisely, the nuclear stopping power of an atom in a cluster is less than the stopping of a single atom. The idea that the front atoms in a cluster penetrate the target and clear the way for the rest of the atoms moving behind was used to explain this effect, also called the "clearing-the-way effect" [24, 25]. This effect was experimentally observed for small boron (20 keV/atom) and silver (up to 30 keV/cluster) clusters implanted into silicon and graphite, respectively [26–28]. On the other hand, it was also predicted that the correlated motion of cluster atoms can cause high-yield electronic excitations in the target thus enhancing the stopping of a cluster under certain conditions [29]. This behaviour was originally called the "vicinage effect" and found playing important role mainly for high-energy implantation.

The surface structures in the form of hillocks, produced due to cluster-surface impacts, have not been extensively studied. To our knowledge, there have not yet been any successful results of MD simulations revealing formation of such surface defects published in the literature. Hillocks were experimentally observed in the case of different impact energies (from keV to GeV) with sizes up to 20 nm in height and with different probabilities compared to the simple crater formation [30–34]. Various attempts to explain the formation of such nanometer sized surface bumps involve thermal spike as well as shock wave, pressure pulse and Coulomb explosion models [32, 35].

Very recently we have also experimentally observed the formation of so-called "complex craters" when hillocks were found to be surrounded by rims of crater walls [36]. In this paper we present the results of systematic studies of these complex structures formed on two different substrate materials, silicon and sapphire, after implantation with low-energy Ar_n^+ and Xe_n^+ cluster ions. Emphasis is placed on the investigation of the effects of different material properties and different cluster species on the mechanism of complex crater formation. After analysis of the collected data, the proposed earlier qualitative model of complex crater formation is developed. Finally, the comparison between our results and the results of different theoretical and experimental studies on similar systems obtained by other groups is presented.

2 Experimental

Samples of Si(111) with a natural oxide layer and Al_2O_3(1-102) were implanted by Ar_n^+ and Xe_n^+ cluster ions obtained using the Pulsed Cluster Source (PUCLUS) setup. The detailed description of PUCLUS can be found elsewhere [37, 38]. Here we only briefly mention the main features of the experimental setup that are relevant to the present studies.

The cluster source is based on a high pressure pulsed valve for supersonic expansion (Even-Lavie-5-2000) mounted on a source chamber with a 3D translator. The typical gas stagnation pressures for Ar and Xe feed gases were 90 and 30 bars, respectively. The pulse repetition rate was 10 Hz. Positively charged cluster ions are efficiently generated by supersonic expansion of gas through the nozzle and its subsequent electron impact ionisation from a hot tungsten filament located on the outlet of the valve. A conical skimmer (orifice diameter 1.9 mm) separates the production and acceleration stages of PUCLUS. The subsequent acceleration, focusing, deflection and mass selection of the cluster ion beam produced by the source take place in the acceleration chamber. An MCP detector for primary cluster ion beam detection and characterisation is mounted in a third (collision) chamber. The samples for implantation are loaded in the collision chamber. The background pressure in the collision chamber was 2×10^{-7} mbar, which rose to 1×10^{-6} mbar after the introduction of the cluster beam. The estimated ion beam fluences during the experiments were around 10^9 cm^{-2} ensuring isolated single cluster impact with the surfaces.

In the first series of experiments, two different types of substrate, Si and Al_2O_3, were both bombarded with Ar_n^+ clusters ($n = 12 \pm 1, 22 \pm 1, 32 \pm 1, 54 \pm 1$). The substrate materials were obtained from *CrysTec* and *Crystal* commercial suppliers [39, 40]. The Si samples had a natural oxide layer with a thickness of ~ 2.5 nm as determined from TEM measurements. The main properties of the two materials are listed in Table 1.

The aim of the second series of experiments discussed here was to investigate the influence of the mass of the cluster monomer units on the surface defect formation. In this case two different sets of rare-gas clusters were chosen to be implanted into one kind of substrate: Ar_n^+ ($n = 12 \pm 1, 22 \pm 1, 32 \pm 1, 54 \pm 1$) and Xe_n^+ ($n = 4, 16$) into Si. The cluster sizes were chosen in such a way that clusters made of Ar and Xe atoms had similar total masses, e.g. $Ar_{12\pm1}^+$ and Xe_4^+. The cluster energy (implantation energy) was varied within the range of 3–18 keV/ion.

Table 1. Material properties data for silicon and sapphire samples.

	SiO_2 / Si	Al_2O_3
Surface orientation	Amorph. / (111) [39]	(1-102) [40]
Density, g/cm^3	2.19 / 2.33 [41]	3.98 [40]
Melting point, K	1986 / 1685 [41]	2325 [40]
Enthalpy of fusion, kJ/mol	- / 50.21 [41]	111.4 [41]
Thermal conductivity (300 K), W/mK	1.4 / 148 [41]	23.1–25.2 [40]
Displacement energy, eV	15 (Si), 20 (O) / 15 (Si) [42]	16 (Al), 75 (O) [43]

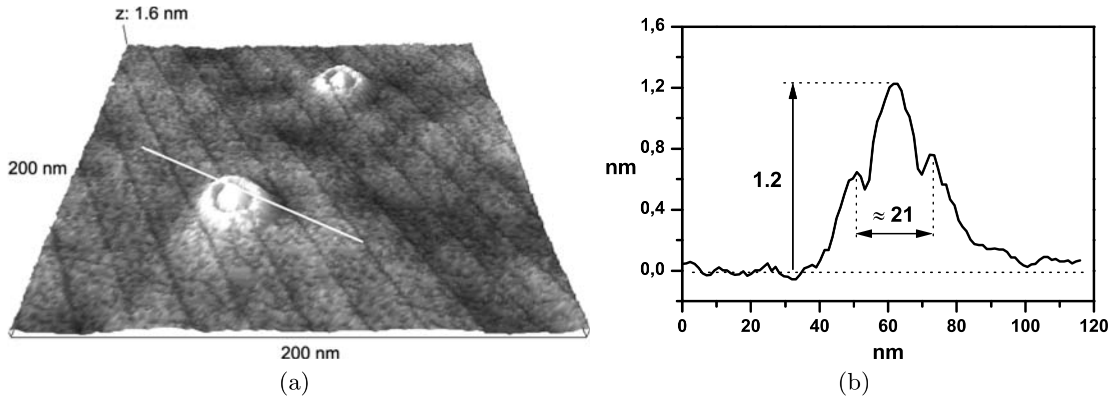

Fig. 1. (a) AFM image of complex craters formed on the surface of silicon after 18 keV $Ar^+_{12\pm1}$ cluster ion implantation; (b) cross-sectional view of one of the complex structures.

AFM was used for analysis of the surface morphology of the implanted samples. The instrument used was a DI Dimension 3000 Scanning Probe Microscope and it was run in the tapping mode. Two cantilevers (both purchased from *MikroMasch*) were used: a standard Si cantilever with a tip curvature radius of less than 10 nm and a Si cantilever with a diamond-like extra tip having a curvature radius of 1 nm. Due to the finite radius of curvature of the tip, nanometer-sized structures are typically imaged with distortion in the lateral dimensions. A relative error of up to 30% can be expected for the measurements of lateral dimensions of features with 10–20 nm in size. The height of the surface defects was measured more precisely with an absolute error $\leq$0.2 nm.

A few selected samples were also studied by SEM and TEM. For SEM analysis a Leo Ultra 55 FEG machine was used with 1 keV electron beam energy, in the secondary electron detection mode. The TEM used was a Philips EM 400 electron microscope equipped with a LaB_6 filament operated at 120 keV for optimum imaging contrast. The samples for TEM were prepared by mechanical thinning, polishing and ion milling from the back side to make the samples electron transparent.

3 Results

3.1 Complex craters

The presence of structures called "complex craters" was observed on the surface of implanted materials in preliminary experiments on implantation of Si by Ar^+_n clusters and Ar^+ ions as well as other cluster-substrate combinations [36, 44]. A typical AFM image of such a defect is shown in Figure 1a. The cross-sectional view is presented in Figure 1b.

On the basis of various theoretical studies and experimental data on cluster-surface impact [18, 20, 21] the following scheme was proposed for the mechanism of complex crater formation: an impacting cluster ion generates multiple collision cascades overlapping with each other in a very narrow surface region of the solid material. The kinetic energy of the cluster constituents is transferred to the substrate atoms mainly via the nuclear stopping mechanism (low-energy cluster implantation). Other effects such as shock-waves as well as efficient ionisation in the material also play an important role in the evolution of defects during the very first picoseconds following the impact. A high density of energy deposition results in a local melting of a shallow layer of the material around the impact spot. Because of the difference in densities of the hot fluidised material and the surrounding crystalline material and also due to local tensions and elastic rebound of the bulk, the liquid melt is pushed away (expulsed) from the surface. The subsequent rapid quenching of the melted material results in the formation of a hillock which is surrounded by the rim of the crater wall. Due to significant material intermixing in the collision spot there is a probability for some of the cluster atoms to get stuck in the target during its re-solidification. Therefore, one can expect that the hillock interior contains cluster atoms alongside small cavities, as indicated by recent MD simulations for Ar_{12} and Ar_{54} cluster implantation into Si(111)

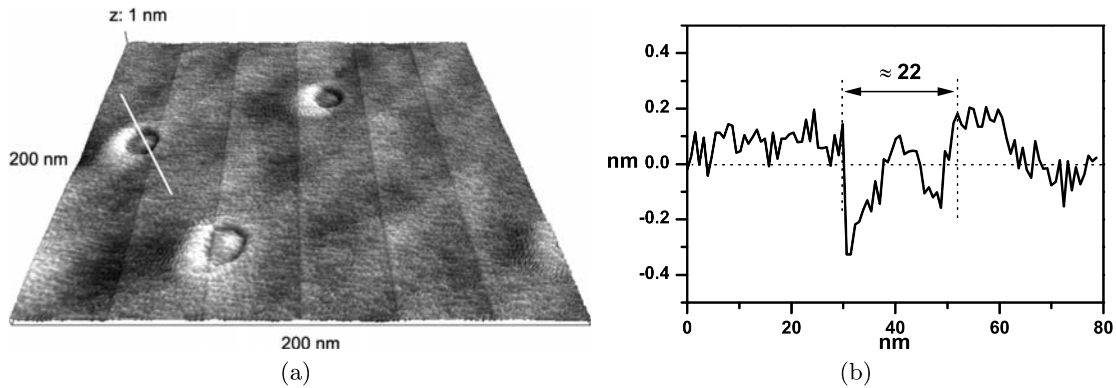

Fig. 2. (a) AFM image of complex craters formed on the surface of silicon after 15 keV $Ar^+_{54\pm1}$ cluster ion implantation; (b) cross-sectional view of the marked crater.

and SiO_2/Si(111) [45]. The simulations showed that a volumetric ratio of the embedded argon atoms is negligible compared to the volume of the collisional cascades formed in SiO_2 and Si.

Here we report the results of systematic studies that show that the height of the central hillock is strongly dependent on the cluster implantation energy, cluster size, type of cluster and type of sample material used for implantation. In the following two sections the experimental results on complex crater formation due to cluster-surface collisions are presented and related to the expectations of the above scenario.

3.2 Defect formation on SiO_2/Si and Al_2O_3 surfaces bombarded with Ar^+_n clusters

The initial surface roughness of the silicon samples before irradiation was found to be below 0.2 nm. The roughness is obtained by AFM on a few randomly chosen areas of 2×2 μm. After bombardment of the silicon samples with 3 keV $Ar^+_{12\pm1}$ clusters, conically shaped hillocks were formed as a result of single cluster-surface impacts. The detailed AFM studies revealed also the presence of rims centered around the hillocks. The mean hillock height and mean basal diameter for this cluster size and implantation energy were estimated from the AFM data to be 2.5 ± 1 nm and 20 ± 5 nm, correspondingly. The surrounding rims were found to be significantly lower with a maximum height of approximately 0.5 nm and a mean diameter of 35 nm. As mentioned above, the lateral dimensions of the hillocks can be enlarged and shapes can be distorted due to tip convolution. The height distribution of hillocks in the range of ±1 nm found in our case can presumably be explained by the statistical longitudinal range straggling of the cluster constituents in the target and effects of energy transfer related to this. It is also possible that variations of the SiO_2 layer thickness can partly contribute to deviations in hillock heights. The presence of simple craters, i.e. ones that do not contain central hillocks, was not found on these samples.

When increasing the implantation energy of $Ar^+_{12\pm1}$ clusters into silicon the following changes in the resulting complex structures were observed: the hillocks were found to be lower in height and narrower in diameter while the crater rim-to-rim diameter stayed approximately the same. At the same time a significant number of simple craters was found. The mean diameter of these craters was 15 nm. A similar effect of hillock disappearance was observed for heavier cluster ions ($Ar^+_{22\pm1}$, $Ar^+_{32\pm1}$, $Ar^+_{54\pm1}$) while increasing the implantation energy. For constant implantation energy a decrease in hillock height with increasing cluster size takes place. The rim-to-rim diameter of complex craters is nevertheless comparable to the one mentioned before. The rate of the simple to the complex crater formation increases with increase of the cluster size. It might also be that the hillocks inside the craters become too small to be resolved by the AFM. In Figure 2 an AFM image of silicon implanted with 15 keV/ion $Ar^+_{54\pm1}$ clusters is shown where the complex structure of the craters has almost vanished. The summary of these studies is presented in Table 2a. The mean values and the standard deviations of the data in the table were obtained from AFM image analysis with data sets of up to 100 measurements per value.

The complex craters were also observed on silicon samples implanted by monomer Ar^+ ions with an energy of 1.5 keV [36, 44]. In this case, hillocks were found to be approximately 1 nm in height and with basal diameters of 15 nm. If one compares these data with those obtained in the case of 18 keV/ion (1.5 keV per atom) $Ar^+_{12\pm1}$ cluster ion bombardment of silicon, one can find that there is a small difference in hillock height for these two cases. It could be accounted for by the clearing-the-way effect. Thus, cluster constituents are expected to penetrate deeper, compared to single monomer ions, producing smaller hillocks. The ratio of simple-to-complex craters was hight for the monomer Ar^+ implantation. Mostly simple craters were also observed by AFM with an increase of the monomer implantation energy (up to 6 keV).

In addition to the extensive AFM studies of the silicon samples implanted by Ar^+_n clusters, several selected samples from this set were also examined by TEM and SEM. In Figure 3 a TEM image (in-plain view) of a single defect produced on silicon by 15 keV $Ar^+_{54\pm1}$ cluster impact is shown. We believe that the circular contrast originates

Table 2. The hillock and crater dimensions obtained from AFM measurements of the samples of (a) silicon bombarded by Ar_n^+ clusters, (b) sapphire bombarded by Ar_n^+ clusters and (c) silicon bombarded by Xe_n^+ clusters.

	cluster size, n	cluster energy, keV	hillock height, nm	hillock diameter, nm	crater rim-to-rim diameter, nm	simple crater diameter, nm
(a)	12 ± 1	3	2.5 ± 1.0	20 ± 5	35 ± 5	not found
		6	2.5 ± 1.0	18 ± 5	35 ± 5	not found
		9	2.2 ± 0.8	18 ± 5	35 ± 5	not found
		12	1.5 ± 0.5	18 ± 5	30 ± 5	15 ± 5
		15	0.7 ± 0.3	15 ± 5	30 ± 5	13 ± 3
		18	0.7 ± 0.3	10 ± 5	20 ± 5	15 ± 5
	22 ± 1	3	1.5 ± 0.5	20 ± 5	35 ± 5	not found
		6	1.5 ± 0.5	unresolved	40 ± 10	30 ± 5
		9	2.0 ± 0.5	15 ± 5	40 ± 10	20 ± 5
		12	0.5 ± 0.2	13 ± 3	25 ± 5	15 ± 5
		15	0.5 ± 0.2	13 ± 3	25 ± 5	15 ± 5
	32 ± 1	3	0.7 ± 0.3	13 ± 3	35 ± 5	12 ± 2
		6	0.7 ± 0.3	unresolved	35 ± 5	12 ± 2
		9	0.7 ± 0.3	15 ± 5	35 ± 5	13 ± 3
		12	0.7 ± 0.3	15 ± 5	30 ± 5	13 ± 3
		15	0.5 ± 0.2	13 ± 3	25 ± 5	12 ± 2
	54 ± 1	4	0.5 ± 0.2	13 ± 3	30 ± 5	12 ± 2
		15	0.5 ± 0.2	12 ± 2	20 ± 5	15 ± 5
(b)	12 ± 1	3	not found	not found	not found	19 ± 3
		6	1.2 ± 0.4	18 ± 8	unresolved	18 ± 3
		9	1.3 ± 0.6	26 ± 6	30 ± 6	not found
		12	1.3 ± 0.8	23 ± 7	38 ± 4	28 ± 4
		18	0.9 ± 0.3	26 ± 7	32 ± 4	23 ± 5
	54 ± 1	3	0.5 ± 0.2	18 ± 2	32 ± 2	26 ± 3
		9	1.7 ± 0.5	22 ± 2	28 ± 2	not found
		12	1.2 ± 0.5	22 ± 5	41 ± 6	28 ± 3
		15	0.9 ± 0.5	19 ± 3	unresolved	30 ± 5
(c)	4	3	1.0 ± 0.4	34 ± 8	42 ± 10	25 ± 3
		6	0.9 ± 0.3	30 ± 9	39 ± 10	26 ± 3
		9	0.9 ± 0.3	31 ± 4	41 ± 7	27 ± 4
		12	0.7 ± 0.2	38 ± 5	50 ± 7	28 ± 4
		15	0.4 ± 0.2	22 ± 5	33 ± 6	28 ± 7
	16	3	0.9 ± 0.4	36 ± 6	52 ± 6	not found
		6	0.8 ± 0.3	21 ± 3	26 ± 4	23 ± 6
		9	0.8 ± 0.2	20 ± 2	30 ± 2	21 ± 6
		12	0.7 ± 0.2	23 ± 3	42 ± 4	26 ± 6
		15	unresolved	unresolved	29 ± 3	26 ± 6

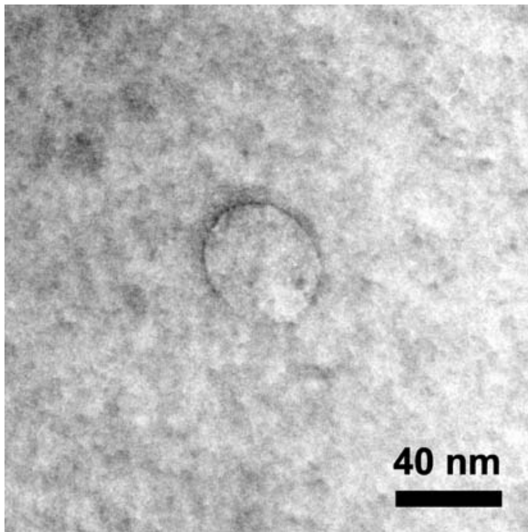

Fig. 3. In-plane TEM image of individual defect formed on the silicon surface after 15 keV $Ar^+_{54\pm1}$ cluster ion implantation.

from the strain and compaction of amorphous material at the border of the region damaged by cluster impact. The contrast appears to be slightly elliptical due to the fact that the crater is viewed at an angle. The diameter of such structures on this particular silicon sample was measured to be approximately 35 nm. No other structural defects extending from the crater walls (like cracks, dislocations, etc.) were found using TEM. It confirms that low-energy cluster implantation can produce very shallow surface damage localised around the point of impact. The result of SEM analysis of silicon samples implanted under similar conditions is illustrated by a typical image in Figure 4. The histogram to the right represents the spot diameter distribution with an average value of 42 nm. The surface density of the observed contrast spots is in good agreement with the density of craters found by AFM. Similar to the TEM studies, no evidence for complex structure of the erosions could be found in the SEM images. The extracted mean diameter of the contrast spots from both the TEM and SEM is slightly larger than the mean rim-to-rim diameter of the complex craters observed on the AFM images (≈30 nm). This difference can presumably be due to different imaging features of the microscopy techniques used and the way the samples were prepared for analysis. The dark spots in SEM and dark rims with faint contrast in TEM presumably correspond to the maximum damaged area due to single cluster impact with no particular details resolved, whereas in AFM we measured the rim-to-rim diameters of the resolved simple and complex craters. The relatively good agreement in the diameter of the craters indicates that the AFM measurements give a realistic indication of the lateral dimensions.

In order to investigate the importance of the properties of the substrate material for understanding the mechanism of complex crater formation, complementary experiments were performed where sapphire samples were bombarded by Ar^+_n cluster ions under identical experimental conditions to the silicon ones. The complex structure of craters was also observed on sapphire by means of AFM (Fig. 5a). Rim-to-rim diameters of the complex and simple craters on sapphire were found to be 30–40 nm and 20–30 nm, correspondingly. While taking into account the uncertainty of the AFM measurements, these data are close to those found for silicon. After analysis of all the irradiated sapphire samples, the complete data set including the data on hillock heights, hillock basal diameters, rim-to-rim diameters of complex as well as simple craters was collected in the Table 2b. Alternatively, the data on hillock height was

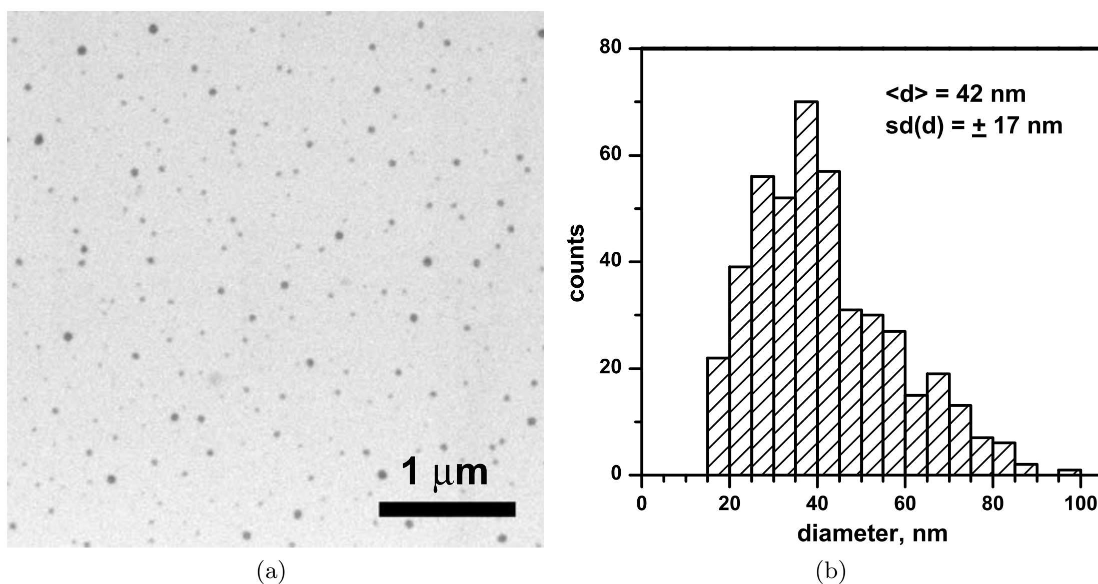

Fig. 4. (a) SEM image of silicon surface after 15 keV $Ar^+_{54\pm1}$ cluster ion implantation and (b) diameter distribution of the contrast spots.

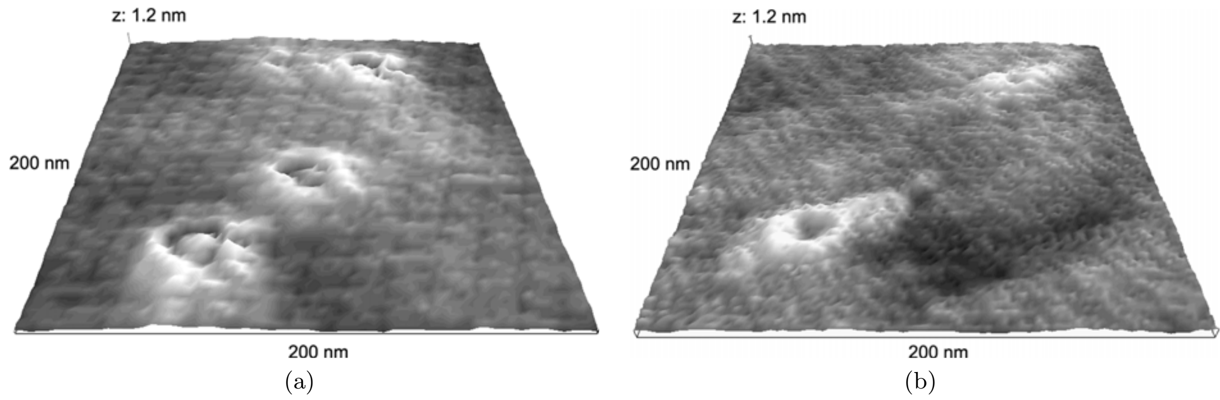

Fig. 5. AFM image of craters formed on the surface of sapphire after (a) 3 keV $Ar^+_{54\pm1}$ and (b) $Ar^+_{12\pm1}$ cluster ion implantation.

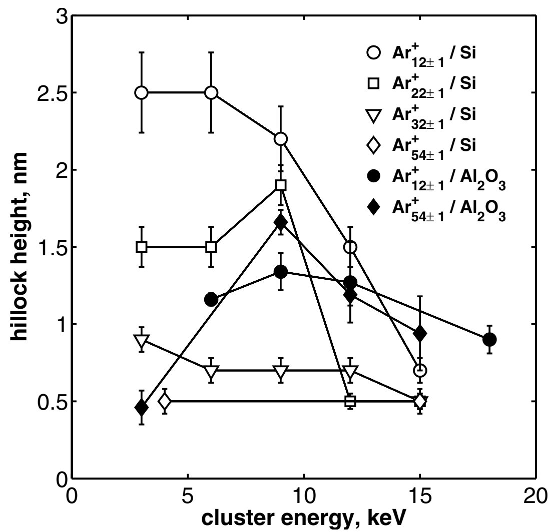

Fig. 6. Hillock height plotted against Ar^+_n cluster ion implantation energies for silicon and sapphire.

plotted against cluster implantation energy for different cluster sizes and for the two substrates used (Fig. 6). The following tendencies for crater and hillock formation were found when comparing the results for both investigated substrates: (1) complex craters appear at higher implantation energies on sapphire than on silicon; (2) for implantation of light clusters ($Ar^+_{12\pm1}$) the hillocks are higher on silicon than on sapphire until the hillocks become comparable in height with the surrounding rims at implantation energies of 15 and 18 keV/ion; (3) there is, in general, a higher rate of formation of simple craters compared to complex craters for sapphire compared to silicon. For example, there were no simple craters found at all on silicon implanted by 3 keV $Ar^+_{12\pm1}$ cluster ions, while for sapphire implanted by the same cluster ions at the same energy, there were no complex craters observed, only simple ones (Fig. 5b).

3.3 Defect formation on SiO_2/Si bombarded with Ar^+_n and Xe^+_n clusters

The importance of the cluster species in the dynamics of cluster collisions with solids was stressed earlier in publications on both experimental and theoretical studies [46,47]. Depending on the size and mass of the individual atom or molecule in the cluster, the binding energy between the cluster constituents and their reactive properties, one can tune the cluster beam to achieve the desired effect during material processing. The cluster species to a large extent define how multi-collisional cascades will develop from the impact spot and whether chemical reaction will take place or not. In the experiment discussed in this section we used two kinds of clusters to investigate the effect of different cluster species on the mechanism of complex crater formation. In both cases clusters were composed of chemically inert elements Ar and Xe and therefore no enhanced chemical surface erosion or other kinds of chemical reactions were expected after cluster impact on silicon. Under other similar implantation conditions (cluster energy, total cluster momentum) the only difference was in the momentum per atom of the cluster.

For Xe-implanted silicon, the same tendency in crater formation as for the Ar-implanted case was found. At the lowest implantation energy of 3 keV/ion mostly complex craters were formed. The rate of formation of simple craters gradually increased with the implantation energy and these types of defects dominated for the heavier clusters (Xe^+_{16}). The mean diameters of simple and complex craters measured from the AFM images for the case of Xe^+_n clusters were found to be 22–28 and 26–52 nm respectively. The complete data set obtained from the AFM measurements is presented in Table 2c and one of the typical AFM images is shown in Figure 7. The data on hillock height are plotted against the cluster energy together with the data on Ar^+_n cluster ion implantation of silicon (Fig. 8). The energy window and the high energy threshold for hillock formation in both cases is quite similar. However, the hillocks produced by Xe^+_4 clusters are found to be almost 2.5 times lower than the ones formed by $Ar^+_{12\pm1}$ clusters.

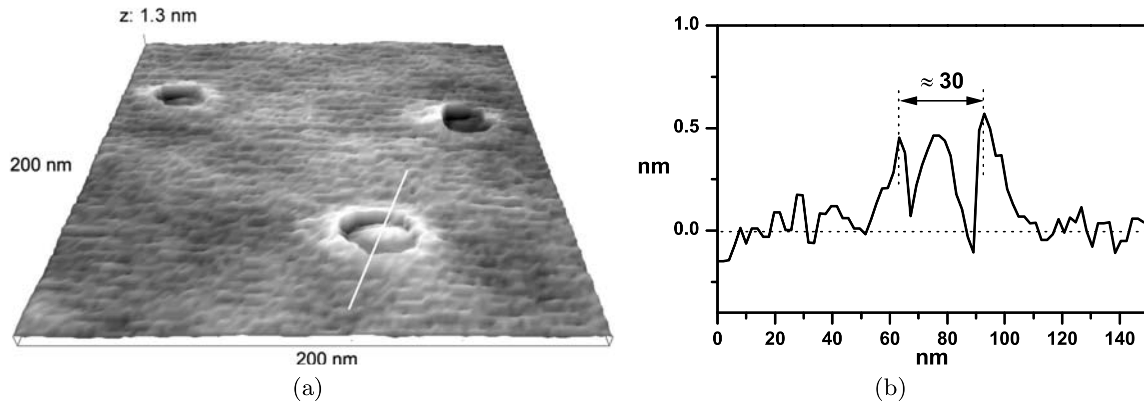

Fig. 7. (a) AFM image of craters formed on the surface of silicon after 6 keV Xe_{16}^+ cluster ion implantation; (b) cross-sectional view of the marked crater.

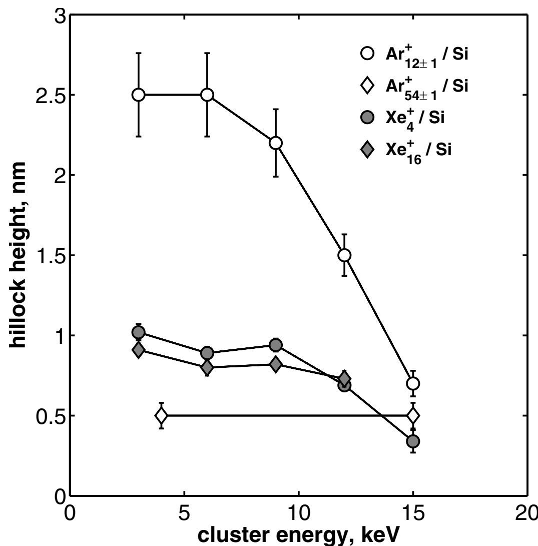

Fig. 8. Hillock height plotted against Ar_n^+ and Xe_n^+ cluster ion implantation energies for silicon.

4 Discussions

As was mentioned in the Introduction, despite numerous MD simulations of cluster-surface collisions with keV energies, there has been no prediction for the formation of significant hillocks. The MD simulations predict a high pressure (∼10 GPa) and temperature (10^4–10^5 K) [18] at the point of the cluster impact that can lead to local melting of the target material. However, the nature of the hillocks presumably resulting from the “expulsion” effect and fast melt quenching is still not well understood.

In terms of radiation damage and energy transfer from a projectile to the material, Al_2O_3 has a higher displacement energy (for both Al and O atoms) compared to SiO_2 and Si (Tab. 1). Sapphire also has a higher melting point and enthalpy of fusion than both crystalline silicon and amorphous silicon oxide materials. Therefore, one would expect that at identical implantation conditions argon cluster ions should produce less locally melted volume at the point of collision on Al_2O_3 than on SiO_2/Si. It might be also important that thermal conductivity of amorphous SiO_2 layer (where major part of the cluster energy is transferred to) is much lower (see Tab. 1) compared to both Si and Al_2O_3. It means that it takes longer for the melt in SiO_2 to cool down and the surface tensions between the molten and solis phase as well as local stress on the boundary SiO_2/Si can lead to significant viscous flows and pushing out the molten material. According to the above described qualitative picture of complex crater formation, the hillocks resulting from molten material quenched after the collision should, in general, be more pronounced on SiO_2/Si compared to Al_2O_3. Such a tendency is seen for implantation energies of argon clusters up to 15 keV/ion in our experiments (Fig. 6). Moreover, from the same figure one can see that the energy window for hillock formation on Al_2O_3 is shifted towards larger values of cluster energies compared to the case of SiO_2/Si. The disappearance of hillocks at higher energies indicates the surface nature of their formation processes, i.e. the cluster-to-target energy transfer processes are shifted deeper into the bulk as the implantation energy increases. It should be also noted that in the case of lowest implantation energy of 3 keV/ion and SiO_2/Si target used in the experiments, the hillocks are probably resulted due to expulsion of the oxide layer. For higher implantation energies, melting of crystalline silicon should be taken into account.

According to the MD calculations presented in [46] (20 keV Ne_n, Ar_n and Xe_n clusters impacting on Si(100)), higher material damage is produced by clusters that carry a larger total momentum at the same cluster energy and cluster size (from tens to a few thousands). Furthermore, in this cluster size range, the effect can be normalised by the total cluster momenta independently of the cluster species. However, in our experiments on hillock formation we clearly see an effect of the cluster species, which means that the momentum of a separate cluster constituent is an important parameter. While analysing the impact of Ar_n^+ and Xe_n^+ clusters with close total mass and the same implantation energy, one can expect higher projected ranges for the xenon constituents due to the higher momentum per cluster atom [26, 27, 42]. Hence, the cluster-to-target energy transfer due to nuclear stopping is shifted slightly

deeper into the substrate for the case of xenon that can lead to a decrease of the surface melting. As mentioned in [47], upon cluster break up, atoms of heavier elements damp the motion of target atoms more efficiently than those of lighter ones. Thus, smaller hillocks by Xe_n^+ cluster ion bombardment can be explained (i) by higher projected ranges of the xenon cluster constituents decreasing surface melting and (ii) by a suppression in the "expulsion" effect due to the damping of the motion of silicon atoms (also oxygen atoms in the oxide layer) by heavy xenon atoms.

5 Conclusions

Results of systematic studies of surface defect formation under various conditions of energetic cluster-surface impact were presented. The formation of simple and complex craters was observed by AFM on the surfaces of silicon and sapphire samples implanted by Ar_n^+ and Xe_n^+ cluster ions.

The effect of the substrate properties on the complex crater formation mechanism was investigated by comparison of the AFM data obtained on SiO_2/Si and Al_2O_3 samples both implanted with the Ar_n^+ cluster ions under identical conditions. More prominent complex craters with higher hillocks were found on silicon substrates that have lower material density, melting temperature and smaller atomic displacement energies compared to sapphire. It was also found that the energy window where hillocks are formed is shifted towards higher implantation energies in the case of sapphire. Cluster implantation into sapphire also leads to a higher rate of simple crater formation compared to silicon.

In addition to the AFM investigations, SEM and TEM analysis was performed on several selected samples of SiO_2/Si implanted by Ar_n^+ clusters. There were no complex structures observed in these studies, however the surface density and diameters of the features were found to be comparable with the ones obtained by AFM on the same samples.

In order to understand the importance of the clusters species for the process of complex crater formation, another comparative study was performed where clusters of different chemical elements, namely argon and xenon, were implanted under similar conditions into SiO_2/Si substrates. In the case of xenon cluster implantation, the produced hillocks were observed to be lower than for the argon cluster implantation. It was suggested that the difference in the projected ranges of argon and xenon cluster constituents and, connected to this, the difference in the total energy losses on the cluster stopping powers leads to a decrease of the energy transfer at the surface layer and therefore also a decrease of the surface melting in the case of xenon cluster implantation. The effect can also be explained in the way that after cluster breakup on impact the more than three times heavier xenon atoms damp the motion of target atoms more efficiently than the argon atoms do, thus decreasing the effect of "expulsion" of the melted material. Such qualitative explanations also agree with the fact that a much higher rate of simple craters was observed for the case of xenon compared to argon cluster implantation.

The authors acknowledge financial support from The Swedish Research Council (VR) and are grateful to Prof. L. Hultman (Linköping University) for possibility of the TEM measurements.

References

1. I. Yamada, J. Matsuo, N. Toyoda, A. Kirkpatrick, Mater. Sci. Eng. R **34**, 231 (2001)
2. R.E. Palmer, S. Pratontep, H.-G. Boyen, Nat. Mater. **2**, 443 (2003)
3. C. Binns, Surf. Sci. Rep. **44**, 1 (2001)
4. A. Perez, P. Melinon, V. Dupuis, P. Jensen, A. Prevel, J. Tuaillon, L. Bardotti, C. Martet, M. Treilleux, M. Broyer, M. Pellarin, J.L. Vaille, B. Palpant, J. Lerme, J. Phys. D **30**, 709 (1997)
5. Y. Qiang, Y. Thurner, T. Reiners, O. Rattunde, H. Haberland, Surf. Coating Tech. **100-101**, 27 (1998)
6. H.-J. Gao, S.J. Pang, Z.Q. Xue, in *Electrical and optical polymer systems*, edited by D.L. Wise, G.E. Wnek, B.J. Trantolo, T.H. Cooper, J.D. Gresser (Marcel Dekker, New York, 1998), p. 729
7. *Metal clusters at surfaces*, edited by K.-H. Meiwes-Broer (Springer, Berlin, 2000)
8. K.L. Merkle, W. Jager, Phil. Mag. A **44**, 741 (1981)
9. F. Seitz, J.S. Koehler, *Solid state physics: advances in research and applications*, edited by F. Seitz, D. Turnbull (Academic, New York, 1956), Vol. 2
10. R. Kelly, Radiat. Eff. **32**, 91 (1977)
11. L. Porte, M. Phaner, C.H. de Villeneuve, N. Moncoffre, J. Tousset, Nucl. Instrum. Meth. Phys. Res. B **44**, 116 (1989)
12. Q. Yang, T. Li, B.V. King, R.J. MacDonald, Phys. Rev. B **53**, 3032 (1996)
13. I.C. Gebeshuber, S. Cernusca, F. Aumayr, H.P. Winter, Int. J. Mass Spectrom. **229**, 27 (2003)
14. A. Audouard, R. Mamy, M. Toulemonde, G. Szenes, L. Thome, Europhys. Lett. **40**, 527 (1997)
15. V.A. Skuratov, D.L. Zagorski, A.E. Efimov, V.A. Kluev, Y.P. Toporov, B.V. Mchedlishvili, Radiat. Meas. **34**, 571 (2001)
16. C. Müller, M. Cranney, A. El-Said, N. Ishikawa, A. Iwase, M. Lang, R. Neumann, Nucl. Instrum. Meth. Phys. Res. B **191**, 246 (2002)
17. G. Szenes, Nucl. Instrum. Meth. Phys. Res. B **191**, 27 (2002)
18. L.P. Allen, Z. Insepov, D.B. Fenner, C. Santeufemio, W. Brooks, K.S. Jones, I. Yamada, J. Appl. Phys. **92**, 3671 (2002)
19. D. Takeuchi, T. Seki, A. Takaaki, J. Matsuo, I. Yamada, Mat. Chem. Phys. **54**, 76 (1998)
20. T.J. Colla, R. Aderjan, R. Kissel, H.M. Urbassek, Phys. Rev. B **62**, 8487 (2000)
21. Y. Yamaguchi, J. Gspann, Phys. Rev. B **66**, 155408 (2002)
22. M. Moseler, O. Rattunde, J. Nordiek, H. Haberland, Nucl. Instrum. Meth. Phys. Res. B **164-165**, 522 (2000)
23. Z. Insepov, R. Manory, J. Matsuo, I. Yamada, Nucl. Instrum. Meth. Phys. Res. B **148**, 47 (1999)

24. Y. Yamamura, Nucl. Instrum. Meth. Phys. Res. B **33**, 493 (1988)
25. V.I. Shulga, M. Vicanek, P. Sigmund, Phys. Rev. A **39**, 3360 (1989)
26. S. Pratontep, P. Preece, C. Xirouchaki, R.E. Palmer, C.F. Sanz-Navarro, S.D. Kenny, R. Smith, Phys. Rev. Lett. **90**, 055503 (2003)
27. L. Seminara, P. Convers, R. Monot, W. Harbich, Eur. Phys. J. D **29**, 49 (2004)
28. J.H. Liang, H.M. Han, Nucl. Instrum. Meth. Phys. Res. B **228**, 250 (2005)
29. N.R. Arista, A. Gras-Marti, J. Phys.: Condens. Matter **3**, 7931 (1991)
30. P. Von Blanckenhagen, A. Gruber, J. Gspann, Nucl. Instr. Meth. Phys. Res. B **122**, 322 (1997)
31. J.-H. Song, S.N. Kwon, D.-K. Choi, W.-K. Choi, Nucl. Instrum. Meth. Phys. Res. B **179**, 568 (2001)
32. M. Döbeli, F. Ames, C.R. Musil, L. Scandella, M. Suter, H.A. Synal, Nucl. Instrum. Meth. Phys. Res. B **143**, 503 (1998)
33. P.A. Thevenard, J.-P. Dupin, B. Vu Thien, S.T. Purcell, V. Semet, Surf. Coating Tech. **128**, 59 (2000)
34. B. Canut, P. Thevenard, C. Jardin, Nucl. Instrum. Meth. Phys. Res. B **218**, 487 (2004)
35. J.C. Girard, A. Michel, C. Tromas, C. Jaouen, S. Della-Negra, Nucl. Instrum. Meth. Phys. Res. B **209**, 85 (2003)
36. V.N. Popok, S.V. Prasalovich, E.E.B. Campbell, Surf. Sci. **566-568**, 1179 (2004)
37. V.N. Popok, S.V. Prasalovich, M. Samuelsson, E.E.B. Campbell, Rev. Sci. Instrum. **73**, 4283 (2002)
38. V.N. Popok, S.V. Prasalovich, E.E.B. Campbell, Nucl. Instrum. Meth. Phys. Res. B **207**, 145 (2003)
39. CrysTec GmbH, `www.crystec.de`
40. Crystal GmbH, `www.crystal-gmbh.com`
41. *CRC Handbook of Chemistry and Physics* edited by D.R. Lide, 81st edn. (CRC Press, Cleveland, 2000)
42. J.F. Ziegler, J.P. Biersack, U. Littmark, *The Stopping and Range of Ions in Solids* (Pergamon Press, New York, 1985)
43. D.M. Parkin, C.A. Coulter, J. Nucl. Mater. **101**, 261 (1981)
44. V.N. Popok, S.V. Prasalovich, E.E.B. Campbell, Vacuum **76**, 265 (2004)
45. J. Samela, K. Nordlund, private communications
46. T. Aoki, J. Matsuo, G. Takaoka, I. Yamada, Nucl. Instrum. Meth. Phys. Res. B **206**, 861 (2003)
47. R. Kramer, Y. Yamaguchi, J. Gspann, Surf. Interface Anal. **36**, 148 (2004)